WO3-decorated ZnO nanostructures for light-activated applications

WO_3-decorated ZnO nanostructures for light-activated applications

Alberto Gasparotto,*[a] Giorgio Carraro,[a] Chiara Maccato,[a] Cinzia Sada,[b] José Balbuena,[c] Manuel Cruz-Yusta,[c] Luis Sánchez,[c] Nives Vodišek,[d] Urška Lavrencic Štangar[d,e] and Davide Barreca[f]

[a] Department of Chemical Sciences, Padova University and INSTM, 35131 Padova, Italy.

[b] Department of Physics and Astronomy, Padova University and INSTM, 35131 Padova, Italy.

[c] Department of Inorganic Chemistry and Engineering Chemistry, Córdoba University, 14071 Córdoba, Spain.

[d] Laboratory for Environmental and Life Sciences, Nova Gorica University, 5001 Nova Gorica, Slovenia.

[e] Faculty of Chemistry and Chemical Technology, Ljubljana University, 1000 Ljubljana, Slovenia.

[f] CNR-ICMATE and INSTM, Department of Chemistry, Padova University, 35131 Padova, Italy.

* Corresponding author; phone: +39-0498275192; e-mail: alberto.gasparotto@unipd.it .

Abstract

In the present work, a two-step vapor-phase route was implemented for the tailored design of ZnO-WO_3 nanoheterostructures supported on fluorine doped tin oxide (FTO) substrates. Under optimized conditions, the sequential use of chemical vapor deposition (CVD) and radio frequency (RF)-sputtering for the deposition of zinc and tungsten oxides respectively, resulted in the growth of calyx-like ZnO nanostructures uniformly decorated by a conformal dispersion of low-sized WO_3 nanoparticles. The target materials were characterized by means of a multi-technique approach, with particular regard to their structural, compositional, morphological and optical properties. Finally, their photocatalytic performances were preliminarily tested in the abatement of NO_X gases (NO and NO_2). Due to the unique porous morphology of the ZnO nanodeposit and the high density of ZnO-WO_3 heterojunctions, WO_3-decorated ZnO revealed appealing De-NO_X characteristics in terms of both degradation efficiency and selectivity. Such features, along with the photoinduced superhydrophilicity and self-cleaning properties of the present nanomaterials, candidate them as promising functional platforms for application in smart windows and building materials for environmental remediation.

Keywords: chemical vapor deposition; RF-sputtering; ZnO-WO_3, De-NO_X, photocatalysis; self-cleaning; water contact angle.

1. Introduction

Zinc oxide (ZnO) is a *n*-type semiconductor (E_G = 3.3 eV), with interesting optical, thermal and electrical characteristics, and a very rich defect chemistry.[1-6] Such features, coupled with its unique flexibility in adopting a large variety of nanoscale morphologies (nanowires, nanoribbons, nanocombs, nanohelices, tetrapods, …), have made ZnO an attractive candidate for optoelectronic and gas sensing applications.[2, 3, 7-11] In addition, ZnO has been proposed as an alternative to the widely studied TiO_2 for light-assisted applications, exploiting, in particular, its photocatalytic activity, photoinduced superhydrophilicity (PSH) and self-cleaning behavior.[9, 12-15] In fact, ZnO displays reactivity and energy band positions similar to titanium dioxide, yet featuring a higher carrier mobility, along with lower cost and toxicity.[4, 10, 16-19] As a consequence, ZnO-based materials have been gaining an increasing importance for a variety of photoassisted processes, especially in the field of environmental remediation.[6, 13, 18, 20-22]

In this context, an ongoing challenge concerns the abatement of NO_X (NO and NO_2) emissions in urban areas, since such pollutants contribute to the generation of acid rain[23, 24] and may severely affect human health even at ppb levels.[10, 17, 25] Up to date, TiO_2 materials have been widely studied for photocatalytic NO_X degradation, whereas the use of ZnO and ZnO-based systems in such fields has been scarcely investigated and undoubtedly requires further attention.[10, 16, 17] It is worth highligting that, in spite of the above advantages, ZnO suffers from two main drawbacks that hinder its use in practical applications, *i.e.* the tendency to photocorrosion and the relatively rapid charge carrier recombination.[8, 20, 26, 27]

To circumvent these obstacles and obtain improved functional performances, a valuable strategy consists in the modification of ZnO with other suitable semiconductors, in order to benefit from additive or synergistic effects originating from the combination of the two materials.[7, 20, 22, 28, 29] Among the possible candidates, WO_3, (E_G = 2.7 eV) presents amenable photocatalytic and optoelectronic properties,[14, 30-32] standing as an appealing candidate in the fabrication of ZnO-based systems for light-assisted applications. The favorable band edge energetics at the ZnO/WO_3

interface is in fact expected to promote an enhanced charge carrier separation, resulting, in turn, in an improved photocatalytic activity.[7, 14, 19, 33] Moreover, WO_3 has an excellent stability against photocorrosion, candidating it as a possible protective agent for the surface decoration of ZnO nanosystems.[14, 30, 34, 35] Finally, WO_3 exhibits a strong affinity towards NO_X, an issue of crucial importance for De-NO_X applications.[31, 36-39]

In order to fully exploit the advantages originating from ZnO and WO_3 coupling, a proper design of the target ZnO-WO_3 systems is imperative to control not only the relative amounts of the two oxides but also the morphology, surface area, defect content and interface quality of the resulting materials, that are directly interrelated with the ultimate functional properties.[6, 14, 26, 30, 40] On this basis, the present study has been devoted to the implementation of a hybrid chemical vapor deposition (CVD) and radio frequency (RF)-sputtering synthetic strategy aimed at obtaining ZnO-WO_3 nanoarchitectures with precise material features in view of photocatalytic applications. At variance from the majority of previous works on ZnO-WO_3 photocatalysts, that have been focused on powdered systems,[13, 14, 21, 26, 27, 33] we report herein on the fabrication of supported WO_3-decorated ZnO nanodeposits, that do not suffer from problems related to the aggregation, separation and secondary pollution of powder photocatalysts.[12, 15, 20, 26, 41] In addition, thanks to the very low WO_3 overall content, the obtained ZnO-WO_3 systems maintain the good optical transparency exhibited by pure ZnO in the Visible spectral range, an important feature for eventual utilization in smart windows and building materials. Finally, the concurrent PSH and self-cleaning properties of the fabricated nanomaterials facilitate washing of nitrite/nitrate ions produced during NO_X degradation along with the photooxidation of eventual organic pollutants, thus avoiding the poisoning of the photocatalyst surface.[16, 25] To the best of our knowledge, the present work is the first report on ZnO-WO_3 systems for De-NO_X applications.

2. Experimental

2.1. Synthesis

ZnO depositions were performed trough a home-made thermal-CVD apparatus consisting of a tubular furnace equipped with a quartz tube hot-wall reactor (internal diameter = 9.5 cm, length of the heated region = 20 cm).[42, 43] In each deposition the adopted Zn precursor, $Zn(hfa)_2TMEDA$ (hfa = 1,1,1,5,5,5-hexafluoro-2,4-pentanedionate; TMEDA = *N*,*N*,*N'*,*N'*-tetramethylethylenediamine), synthesized according to the literature,[9] was placed in an external glass vaporizer heated at 80°C, and delivered to the reaction chamber by an electronic grade N_2 flow (rate: = 100 sccm). Gas lines were maintained at 120°C by means of external heating tapes to prevent condensation phenomena. An additional electronic grade O_2 gas flow (rate = 30 sccm) was separately delivered to the reactor through a dedicated line after passing through a water reservoir maintained at 30°C. Prior to each deposition, FTO-coated glass substrates (Aldrich®, 735167-1EA, ≈7 Ω/sq, dimensions = 2.0 cm^2 FTO thickness = 600 nm), were cleaned by dipping in an aqueous solution of sulphonic detergent, rinsing in distilled water, then 1,2-dichloroethane and 2-propanol, and finally dried under an air flow. After preliminary experiments aimed at the optimization of preparative conditions and at the obtainment of an optimal reproducibility, the substrates were placed at the center of the reactor, and ZnO deposition was carried out at 300°C at a total operating pressure of 3.0 mbar (deposition time = 2 h). Such a growth temperature, lower than the one reported in our recent paper,[40] was adopted since, under the present conditions, the formation of ZnO nanostructures with higher porosity and a unique calyx like morphology took place. These features are extremely favorable to maximize WO_3 dispersion during the sputtering process, as well as to provide a high active area available for the catalyst interaction with the target gases during De-NO_X degradation.

For the preparation of ZnO-WO_3 nanomaterials, the above ZnO matrices were fixed on the ground electrode of a previously described two-electrode RF-sputtering reactor (ν = 13.56 MHz).[43] Experiments were performed using electronic grade Ar plasmas, starting from a WO_3 target (Neyco®, purity = 99.99%, thickness = 2 mm, diameter = 2 in.) fixed on the RF-electrode.

Sputtering experiments were carried out using the following optimized conditions:[40] inter-electrode distance = 5 cm; Ar flow rate = 10 sccm; total pressure = 0.3 mbar; RF-power = 20 W; ground electrode temperature = 60°C; deposition time = 3 h.

2.2. Characterization

The overall deposit mass was evaluated by using a Mettler Toledo XS105DU Microbalance. The average weight of the active material on each substrate was estimated to be (0.10 ± 0.02) mg.

X-ray diffraction (XRD) measurements were run at a fixed incidence angle of 1.0° by means of a Bruker D8 Advance instrument equipped with a Göbel mirror, using a CuKα X-ray source (λ = 1.54056 Å).

Field emission-scanning electron microscopy (FE-SEM) analyses were performed by a Zeiss SUPRA 40 VP instrument, using a primary beam voltage of 20.0 kV and collecting electron signals by means of InLens and AsB detectors. Scanning transmission electron microscopy (STEM) micrographs were acquired on the same instrument with an acceleration voltage of 20.0 kV. The ImageJ® (http://imagej.nih.gov/ij/ accessed May 2017) picture analyzer software was used to estimate the average particle size and deposit thickness.

Atomic force microscopy (AFM) analyses were performed by an NT-MDT SPM solver P47H-PRO apparatus, operating in semi-contact mode and in air. Root-mean-square (RMS) roughness values were obtained from 5×5 μm^2 images after background subtraction and plane fitting.

X-ray photoelectron spectroscopy (XPS) analyses were carried out on a Perkin-Elmer Φ 5600ci spectrometer, using a non-monochromatized MgKα excitation source (hν = 1253.6 eV), at a working pressure lower than 10^{-8} mbar. The reported binding energies (BEs) were corrected for charging by assigning a BE of 284.8 eV to the C1s line of adventitious carbon.[44] After a Shirley-type background subtraction, atomic percentages (at.%) were calculatedby integration of

photoelectron signals using sensitivity factors provided by Φ V5.4A software.Calculation of the surface tungsten molar fraction (X_W) was performed according to the following relation:[24, 45]

$$X_W = (W\ at.\%)\times 100/[(W\ at.\%) + (Zn\ at.\%)] \quad (1)$$

where W at.% and Zn at.% are the tungsten and zinc atomic percentages, respectively.

Secondary ion mass spectrometry (SIMS) investigation was carried out by a IMS 4f mass spectrometer (Cameca), using a Cs^+ primary beam (voltage = 14.5 keV; current = 30 nA, stability = 0.3%) and negative secondary ion detection, adopting an electron gun for charge neutralization. Measurements were performed in beam blanking mode and high mass resolution configuration. Signals were recorded rastering over a 150×150 μm^2 area and detecting secondary ions from a sub region close to 7×7 μm^2 in order to avoid crater effects.

Optical absorption spectra were collected in transmission mode at normal incidence by means of a Cary 50 spectrophotometer. In all cases, the substrate contribution was subtracted. Tauc plots were extrapolated from the recorded spectra, assuming the occurrence of direct allowed electronic transitions.[40, 45]

2.3. Functional tests

Photocatalytic De-NO_X experiments were performed at room temperature using a protocol similar to the standardized one developed for the characterization of air-purification performances.[24] In particular, taking into account the sample geometric area (2.0 cm^2) and the low average deposit mass [(0.10 ± 0.02) mg], a small-sized quartz reactor (volume = 7 cm^3) and a NO concentration of 150 ppb were chosen, in order to achieve an optimal sensitivity. The reactor was placed inside a light sealed irradiation box (Solarbox 3000e RH) equipped with a Xe lamp for sample irradiation with artificial sunlight (25 and 550 $W\times m^{-2}$ for UV and Vis irradiance, respectively). The target NO concentration was obtained by mixing pure NO with synthetic air (flow rate = 0.3 $L\times min^{-1}$), previously conveyed to a gas-washing bottle filled with demineralised water in order to maintain a

constant relative humidity of 50±5 %. The accurate measurement of nitrogen oxides concentrations was carried out using a chemiluminescence analyser (model Environment AC32M). For each test, the air/NO gas flow was preliminarily passed over the sample in the dark for a period of 10 min. Subsequently, irradiation was switched on for 60 min. Tests were repeated three times to obtain average concentration values. The calculated standard deviations are ± 0.3 ppb for NO concentration, and ± 1.0 ppb for NO_2 and NO_X ones.

Evaluation of terephthalic acid (TPA) photocatalytic degradation was carried out by the following procedure. A TPA solution (40 mL, 0.015 $g \times L^{-1}$) was transferred into a photoreactor cell consisting of a glass beaker with diameter of *ca.* 40 mm. Specimens were mounted horizontally on a polytetrafluoroethylene sample holder and immersed in the TPA solution under magnetic stirring. The beaker was covered with a borosilicate Petri dish to prevent the solution evaporation inside the illumination chamber, that was equipped with UV-A lamps (λ_{max} = 365 nm, 2.29 $mW \times cm^{-2}$). For photocatalytic tests, the solution was first kept in contact for 30 min with the sample under stirring in the dark. Subsequently, the solution was analyzed by fluorescence measurements using a microtiter plate reader spectrofluorometer (Infinite F200 Microplate Reader, Tecan).[46, 47] The concentration of hydroxyterephthalic acid (HTPA), a highly fluorescent product of TPA photocatalytic oxidation, was monitored every 30 min of UV illumination.

Water contact angle (WCA) measurements (Contact Angle Meter CAM-100, KSV Instruments) were performed to study the hydrophobic-to-hydrophilic conversion of the sample surface upon UV-A irradiation. The illumination chamber and UV source were the same used for TPA photocatalytic degradation test. For each irradiation time, WCA values were measured in three different regions of each sample. After completing the analysis and keeping the specimen few days in the dark in order to restore the initial WCA values, measurements were repeated, yielding a very good reproducibility of WCA results. A sample of commercial self-cleaning glass Pilkington Activ™ was used as a reference.

3. Results and discussion

As anticipated, ZnO-WO_3 nanostructures were grown on FTO-coated glass slides by a sequential CVD/RF-sputtering route. The advantages of the adopted synthetic approach have already been explained in our previous works.[24, 43, 48] In the following, the characteristics of a ZnO-WO_3 system prepared under optimized conditions (see Experimental section) are discussed and compared to a reference ZnO specimen. As a matter of fact, both deposits were uniform and well adherent to the substrate, as confirmed by the scotch-tape test.

For the bare ZnO sample, XRD analyses (Fig. 1a) evidenced, besides reflections from the FTO substrate, peaks at 2ϑ = 31.7°, 34.4°, 36.2° and 47.5°, ascribed to the (100), (002), (101) and (102) planes of the *wurtzite* ZnO phase.[49] The ZnO-WO_3 pattern was very similar to the previous one and no additional diffraction peaks attributable to WO_3 could be clearly observed. Such a result, that enabled to rule out the possible formation of Zn-W-O ternary phases,[40, 43] could be explained considering the mild conditions adopted for WO_3 sputtering (see Experimental), yielding a low WO_3 amount and enabling to preserve the structural features of the underlying ZnO system.

For both specimens, the intensity ratio between the (002) and (101) reflections was higher than the reference powder material,[49] indicating a ZnO preferential orientation along the <001> crystallographic direction. Such a result, in line with previously reported data on ZnO nanomaterials,[3, 9, 12] can be rationalized considering the unique calyx-like morphology of the obtained ZnO nanostructures, as evidenced by FE-SEM images (see below).

The system surface composition was investigated by XPS. Survey spectra were dominated by zinc and oxygen photopeaks (Fig. S1), along with a modest surface contamination from aliphatic carbon species arising from atmospheric exposure. In the case of ZnO-WO_3 system, the W4f peak was also clearly detectable. This finding suggests that tungsten sputtering did not result in a complete coverage of the zinc oxide matrix. Accordingly, calculation of the tungsten molar fraction yielded a value of 46.0 %. This result suggested a comparable content of zinc and tungsten species on the

sample surface, a desirable goal to maximize synergistic interfacial effects originating from the coupling of ZnO and WO_3.

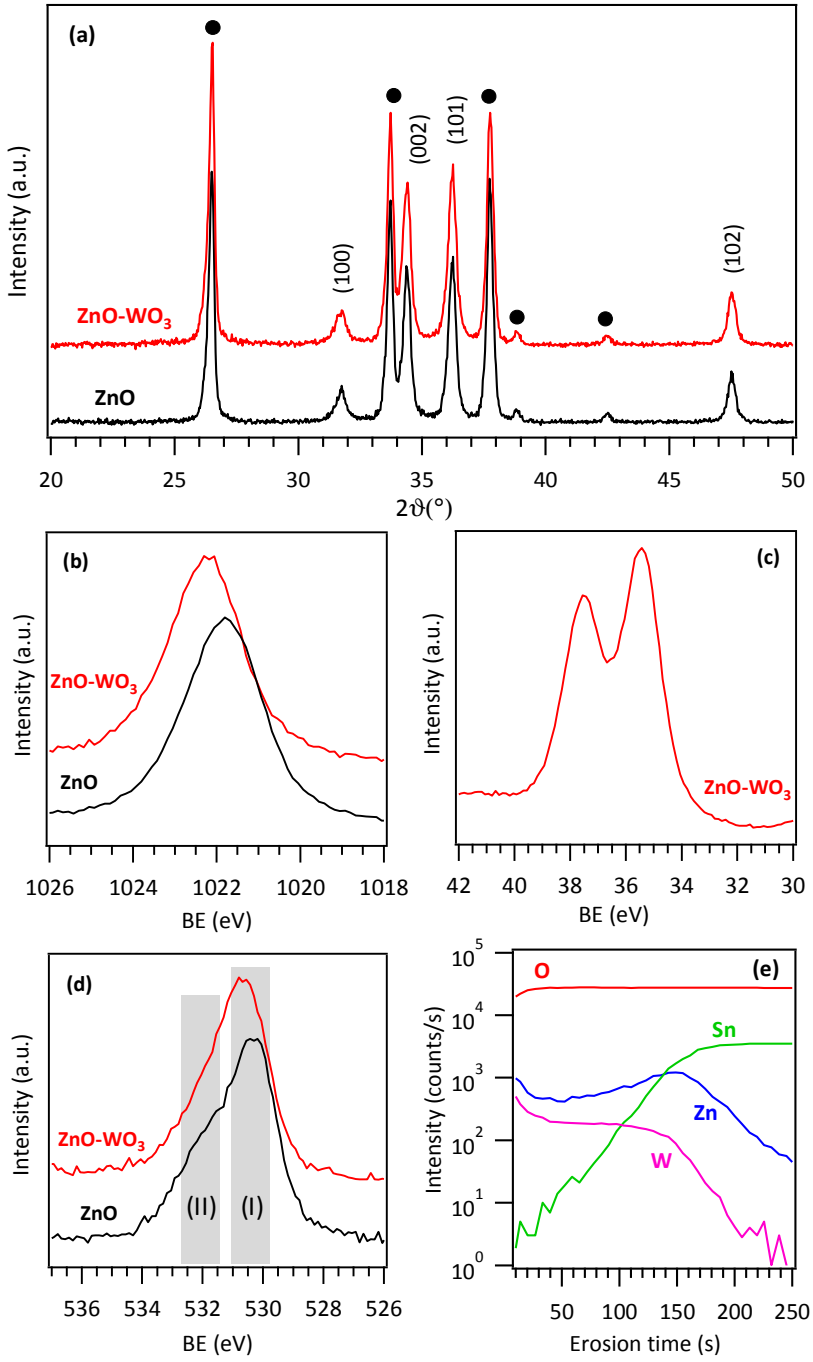

Fig. 1(a) XRD patterns of bare ZnO and ZnO-WO_3 specimens. Reflections from the FTO substrate are marked by circles (●). (b) $Zn2p_{3/2}$, (c) W4f, and (d) O1s XPS surface regions. (e) SIMS depth profile for a ZnO-WO_3 specimen.

Interestingly, whereas for bare ZnO the $Zn2p_{3/2}$ signal was located at 1021.8 eV (Fig. 1b), in good agreement with values expected for zincite, in the case of ZnO-WO_3 the peak was shifted to BE *ca.* 0.5 eV higher.[9, 40, 50-52] This phenomenon indicated the occurrence of an electronic interplay at the ZnO-WO_3 interface. In particular, since the ZnO conduction band edge is positioned at higher energies than the WO_3 one, the coupling of the two semiconductors results in an electron transfer from ZnO to WO_3,[7, 21, 22, 27, 33, 35] explaining thus the $Zn2p_{3/2}$ BE shift to higher values. Conversely, due to the described electron flow, the $W4f_{7/2}$ BE (35.5 eV, Fig. 1c), though compatible with W(VI) in an oxide environment, was slightly lower than typical literature values usually reported for pure WO_3.[32, 38, 50, 53-55]

The O1s signal (Fig. 1d) displayed similar features for the analyzed specimens. Whereas the main component (I) centered at 530.3 eV can be ascribed to lattice oxygen in ZnO and eventually WO_3, the broad shoulder (II) at 532.0 eV arises from hydroxyl groups originating from the chemisorption of atmospheric moisture on the material surface.[22, 35, 53, 56]

The in-depth chemical composition of the ZnO-WO_3 system was investigated by SIMS (Fig. 1e), devoting special attention to the mutual zinc and tungsten distribution. The oxygen ionic yield appeared nearly constant from the surface down to the interface with the FTO substrate, whereas the broadening of the Sn signal was attributed to the high substrate corrugation. As can be observed, the in-depth distribution of tungsten was nearly parallel to the zinc one, suggesting that WO_3 presence was not limited to the system surface, but uniformly extended even into the inner regions. This effect could be traced back to an efficient in-depth dispersion of WO_3 into the porous ZnO deposit, further favored by the inherent infiltration power characterizing RF-Sputtering.[45, 48] The efficient intermixing of the two oxides, resulting in an intimate ZnO/WO_3 contact, is likely to beneficially affect the system functional behavior, since it involves the formation of a high density of heterojunctions.

Figs. 2a-b display the plane-view and cross-sectional morphology of bare ZnO. The deposit was composed by an array of calyx-like structures with hexagonal heads, whose interconnection

produced a rough, porous layer with a thickness of (180±15) nm, conformally covering the underlying FTO substrate. The average in-plane size of individual calyx-like nanostructures was (125±25) nm, while their edge thickness corresponded to (7±1) nm.

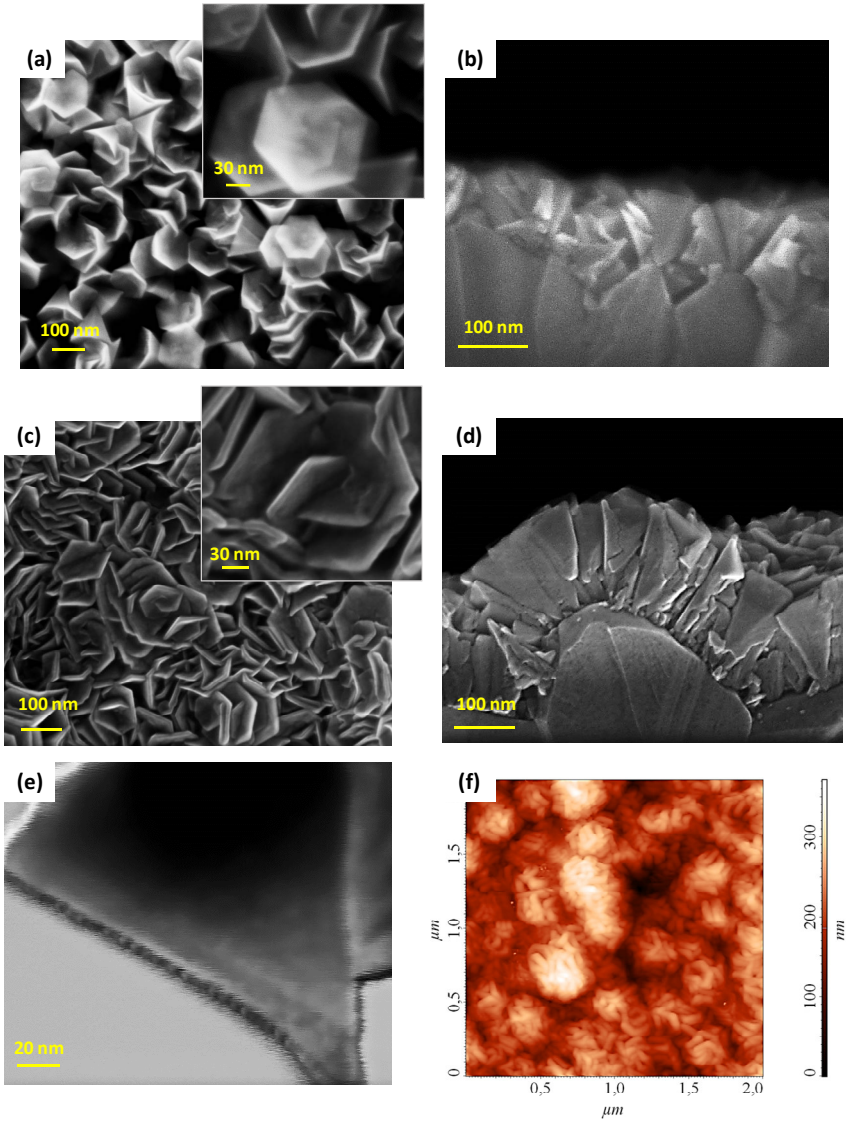

Fig. 2 Plane-view (left) and cross-sectional (right) FE-SEM images of (a,b) bare ZnO and (c,d) ZnO-WO_3 samples. Representative STEM (e) and AFM (f) micrographs of a ZnO-WO_3 specimen.

Upon WO_3 deposition (Fig. 2c and 2d) the system organization did not undergo any major alteration, an effect attributable to the use of mild sputtering conditions and the concomitant deposition of a very low tungsten amount, in line with the above discussed XRD and XPS data. An inspection of high magnification STEM images (Fig. 2e) evidenced the conformal decoration of

ZnO by closely spaced and uniformly distributed WO_3 particles, with an almost spherical shape and an average diameter of (3.7±0.5) nm.

The even dispersion of WO_3 over ZnO was further corroborated by the uniform image contrast of the FE-SEM micrograph reported in the right panel of Fig. S2, that was recorded by collecting backscattered electrons (enhancing thus *Z*-contrast difference between ZnO and WO_3).

AFM analyses (Fig. 2f) revealed very similar morphology and roughness values (RMS roughness ≈55 nm) for both ZnO and ZnO-WO_3, suggesting thus a comparable active area for the two specimens. This result enabled to rule out any significant surface roughness influence on the sample performances in photocatalytic NO_X degradation, that were thus interpreted basing on the occurrence of synergistic effects originating from the coupling of the two semiconductors (see below).

For both ZnO and ZnO-WO_3 systems, optical absorption analyses (Fig. 3) revealed a high transparency in the Vis range and an absorption onset for $\lambda < 380$ nm, as expected for ZnO interband transitions.[6, 17, 28, 33, 51, 57]

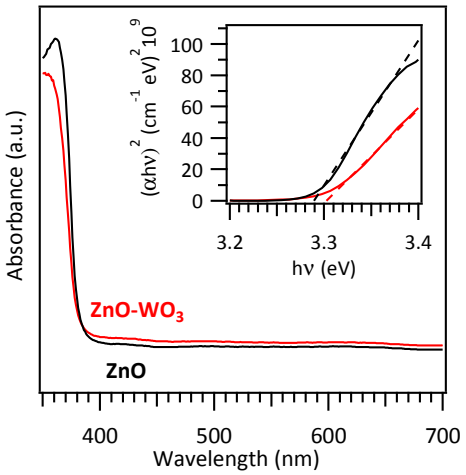

Fig. 3 Optical absorption spectra for ZnO and ZnO-WO_3 samples. The inset displays the correponding Tauc plots.

As can be observed, WO_3 introduction did not result in any appreciable spectral variation with respect to bare ZnO, in agreement with zinc(II) oxide predominance in the developed ZnO-WO_3

systems. Accordingly, irrespective of WO_3 presence, Tauc plot analysis (inset to Fig. 3) yielded very similar band-gap values [E_G = (3.29±0.02) eV] for the two specimens. Such results are perfectly in line with literature data for pure ZnO[5, 6, 51, 56, 58, 59] and confirm the absence of Zn-W-O ternary phases and/or ZnO doping by W species,[30, 60] as also supported by the obtained XRD and XPS results.

The main results obtained in photocatalytic NO_X degradation experiments, performed under a continuous NO supply of 150 ppb, are summarized in Fig. 4.

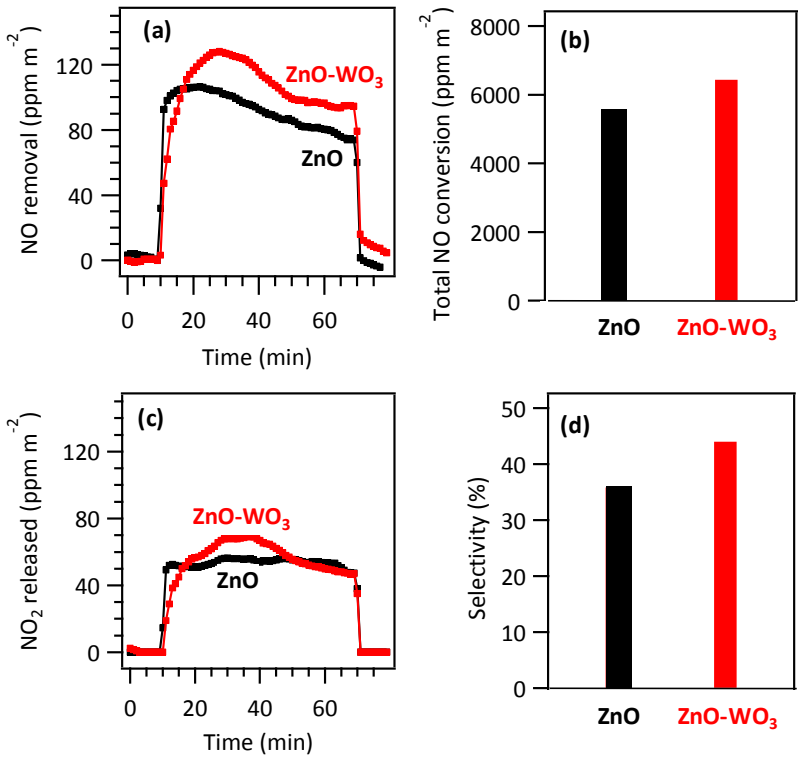

Fig. 4 (a) NO removal as a function of time and (b) corresponding total NO conversion for the target ZnO and ZnO-WO_3 samples. (c) Concentration profiles of NO_2 released during NO photodegradation and (d) NO abatement selectivity for the same specimens.

Under dark conditions (first 10 min of Fig. 4a), NO removal was negligible, clearly evidencing that light exposure was essential to trigger the process. Conversely, upon switching on artificial sunlight irradiation, NO removal rapidly increased for both samples and approached a nearly constant value after ≈50 min of illumination, especially for ZnO-WO_3, indicating the achievement of a relatively stable activity. In spite of the very low WO_3 content, ZnO-WO_3 exhibited a removal efficiency *ca.*

15% higher than bare ZnO, as better evidenced by the integral NO conversion data reported in Fig. 4b. Such an effect can be traced back to a more effective separation of charge carriers originating from the intimate ZnO/WO_3 coupling in the target systems,[7, 13, 19] resulting, in turn, in the suppression of detrimental electron-hole recombination phenomena. Despite ZnO-WO_3 was more active than bare ZnO in NO photooxidation, the formation of comparable NO_2 amounts was observed for both systems (Fig. 4c). It is worthwhile mentioning that the full NO_X removal from air proceeds through the complete photochemical oxidation (PCO) of NO to nitrate ions, a complex process involving several intermediate species.[25, 61] A possible PCO mechanism accounting for the target process after electron-hole pairs formation in ZnO-based materials can be described according to the following reactions:[10]

$$ZnO + h\nu \rightarrow ZnO^{*} (h_{VB}^{+} + e_{CB}^{-}) \quad (2)$$

$$h_{VB}^{+} + H_2O \rightarrow \cdot OH + H^{+} \quad (3)$$

$$e_{CB}^{-} + O_2 \rightarrow \cdot O_2^{-} \quad (4)$$

$$\cdot O_2^{-} + H^{+} \rightarrow \cdot OOH \quad (5)$$

$$NO + 2 \cdot OH \rightarrow NO_2 + H_2O \quad (6)$$

$$NO_2 + \cdot OH \rightarrow NO_3^{-} + H^{+} \quad (7)$$

$$NO_X + \cdot O_2^{-} \rightarrow NO_3^{-} \quad (8)$$

Since NO_2 is significantly more dangerous than NO, its formation as intermediate is highly undesired.[62] As a consequence, an optimal De-NO_X photocatalyst should not only ensure an efficient NO conversion but also an appreciable selectivity, so as to minimize the amount of photooxidized NO released back into the atmosphere as the highly toxic NO_2.[24, 39] Hence, the photocatalysts developed in this work were evaluated also in terms of selectivity, *S* (%), determined according to equation (9):[24]

$$S\ (\%) = \{([NO_X]_{in} - [NO_X]_{out}) / [NO_X]_{in}\} \times 100 / \{([NO]_{in} - [NO]_{out}) / [NO]_{in}\} \quad (9)$$

As shown in Fig. 4d, ZnO-WO_3 was *ca.* 10% more selective than ZnO in promoting the complete NO photooxidation. Total NO_X removal values (calculated by subtracting the amount of released NO_2 from the NO removal value) were estimated to be 2960 and 2300 ppm×m^{-2} for ZnO-WO_3 and bare ZnO respectively, highlighting a beneficial performance improvement induced by functionalization with WO_3.

The enhanced selectivity of the PCO process displayed by ZnO-WO_3 with respect to bare ZnO (see Fig. 4d) is explained basing on the above proposed mechanism, according to which photogenerated holes and electrons (h_{VB}^+/e_{CB}^-), •OH radicals and NO_2 gaseous molecules play a key role in driving the overall process. The high density of heterojunctions in ZnO-WO_3 systems (see above) can be considered as the main effect responsible for the suppression of electron-hole recombination. As a consequence, the formation of strong oxidant reactive oxygen species (ROS) according to reactions (3) and (4) is enhanced, and, in turn, a more effective completion of the $NO \rightarrow NO_2 \rightarrow NO_3^-$ oxidation process is favored. In addition, WO_3 is well known for its adsorption ability towards gaseous NO_X,[31, 36-39] with a beneficial effect on reactions (6) - (8). In particular, the NO_2 conversion to NO_3^- is promoted not only by the more efficient uptake of NO_2 molecules on WO_3-containing systems, but also by the already mentioned ZnO/WO_3 heterojunctions that, under illumination, enable the transfer of photogenerated electrons from ZnO to WO_3. As a consequence, and thanks also to the high electron affinity of NO_2, the latter drains electrons from WO_3 conduction band, yielding the formation of NO_2^- species.[38, 39] Alternatively, NO_2 can be photooxidised to NO_3^- species, as described by equation (7).

As a final remark on De-NO_X tests, it is worth highlighting that ZnO-WO_3 samples prepared with a sputtering time of 5 h, containing a higher WO_3 amount, displayed a degradation efficiency comparable to the above mentioned system, but an appreciably lower selectivity (data not reported). Such a finding clearly indicates that functional properties are improved by maximizing the dispersion of WO_3 particles, rather than merely increasing its content.

The fabricated ZnO-WO_3 nanomaterials display an appreciable activity even in the photodegradation of organic pollutants, as revealed by monitoring the progressive oxidation of TPA, a model contaminant,[12, 52] under UV irradiation. To this regard, Fig. 5a displays the increase of HTPA (one of the products arising from TPA oxidation) concentration *vs.* time. As can be observed, the curve reaches a plateau after 150 min of illumination, as a result of the subsequent HTPA conversion to other products as the photocatalytic oxidation progresses.[12] Fitting of the experimental data was performed using a simplified kinetic model for HTPA to obtain its formation rate constant k_1.[46, 47] Comparison with benchmark Pilkington Activ™ TiO_2 (see also Fig. S3) revealed similar degradation kinetics and k_1 formation rate constants, yielding values of 7.79×10^{-9} and 7.03×10^{-9} $M\times min^{-1}$ for ZnO-WO_3 and Pilkington TiO_2, respectively. Such a behavior represents an important issue for the implementation of the developed De-NO_X nanosystems as functional coatings for smart windows and building materials, in which the present self-cleaning properties ensure that the catalyst surface is always freshly available for the interaction with the target gases, preventing thus a progressive degradation of the catalyst performances under prolonged utilization.

Preliminary WCA tests on ZnO-WO_3 systems (Fig. 5b) revealed an efficient hydrophobic-to-superhydrophilic conversion upon UV irradiation. The progressive increase of surface wettability upon protracted illumination can be traced back to the concomitant degradation of organic species and light-assisted generation of hydroxyl groups, concurring to the observed WCA decrease.[12, 15] It is worth observing that bare ZnO showed a very similar WCA evolution with irradiation time (Fig. S4), indicating that the intrinsic photoinduced superhydrophilicity of ZnO is preserved even upon WO_3 deposition. Interestingly, the PSH behavior of ZnO-WO_3 systems is a further additional benefit for the above De-NO_X applications since it results in an easier washing of nitrite/nitrate ions (*e.g.* by rain), that could otherwise poison the photocatalyst surface, with detrimental effects on its degradation efficiency.[16, 63]

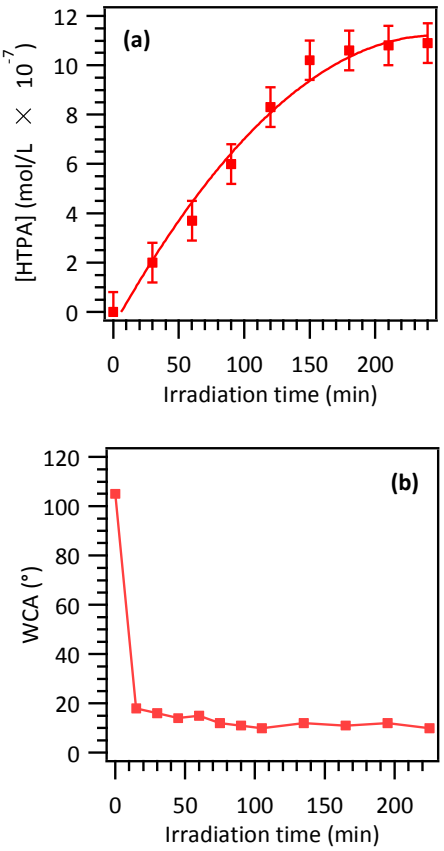

Fig. 5 (a) HTPA concentration and (b) WCA evolution as a function of UV irradiation time for WO_3-decorated ZnO nanosystems.

4. Conclusions

In summary, the present work has reported on the tailored synthesis of WO_3-decorated ZnO calyx-like nanostructures by means of a hybrid CVD/RF-sputtering preparation route. Thanks to the highly porous ZnO morphology and the efficient surface and in-depth dispersion of very small WO_3 nanoparticles, tailored nanomaterials featuring an intimate ZnO/WO_3 contact and a high density of ZnO-WO_3 heterojunctions, were effectively developed. Such characteristics were responsible for the suppression of detrimental electron-hole recombination processes, resulting, in turn, in promising De-NO_X photocatalytic performances that, along with the reported self-cleaning behavior and light-driven superhydrophilicity, candidate the present systems as appealing functional coatings for building materials aimed at environmental remediation. In this regard, it is worth highlighting

that the developed coatings involve the deposition of a minimal WO_3 amount on the fabricated ZnO porous deposits. As a consequence, the present ZnO-WO_3 nanoheterostructures enable to preserve the initial aspect (color, transparency, …) of the underlying substrate. Finally, the proposed nanofabrication strategy can be readily extended and adapted to a variety of supports, as well as to the fabrication of other heteroarchitectures for a plethora of functional end-uses, from light-activated applications to gas sensing. Efforts in this direction are already under way.

Conflicts of interest

There are no conflicts to declare.

Acknowledgements

The research leading to these results has received financial support from Padova University ex-60% 2015-2017, P-DiSC #SENSATIONAL BIRD2016-UNIPD projects and ACTION post-doc fellowship. The authors also kindly acknowledge Dr. Rosa Calabrese (Department of Chemical Sciences, Padova University, Italy) for experimental assistance. Slovenian authors acknowledge Slovenian Research Agency for financial support.

References

1. J. Anderson and G. V. d. W. Chris, *Rep. Prog. Phys.*, 2009, **72**, 126501.
2. L. Schmidt-Mende and J. L. MacManus-Driscoll, *Mater. Today*, 2007, **10**, 40-48.
3. D. Bekermann, A. Gasparotto, D. Barreca, L. Bovo, A. Devi, R. A. Fischer, O. I. Lebedev, C. Maccato, E. Tondello and G. Van Tendeloo, *Cryst. Growth Des.*, 2010, **10**, 2011-2018.
4. F.-H. Ko, W.-J. Lo, Y.-C. Chang, J.-Y. Guo and C.-M. Chen, *J. Alloys Compd.*, 2016, **678**, 137-146.
5. S. Xu and Z. L. Wang, *Nano Res.*, 2011, **4**, 1013-1098.
6. X. Zhang, J. Qin, Y. Xue, P. Yu, B. Zhang, L. Wang and R. Liu, *Sci. Rep.*, 2014, **4**, 4596.
7. F. Zheng, H. Lu, M. Guo, M. Zhang and Q. Zhen, *J. Mater. Chem. C*, 2015, **3**, 7612-7620.
8. L. I. Ali, S. A. El-Molla, M. M. Ibrahim, H. R. Mahmoud and M. A. Naghmash, *Opt. Mater.*, 2016, **58**, 484-490.
9. D. Barreca, A. P. Ferrucci, A. Gasparotto, C. Maccato, C. Maragno and E. Tondello, *Chem. Vap. Deposition*, 2007, **13**, 618-625.
10. Y. Wei, Y. Huang, J. Wu, M. Wang, C. Guo, D. Qiang, S. Yin and T. Sato, *J. Hazard. Mater.*, 2013, **248**, 202-210.
11. D. Barreca, D. Bekermann, E. Comini, A. Devi, R. A. Fischer, A. Gasparotto, C. Maccato, C. Sada, G. Sberveglieri and E. Tondello, *CrystEngComm*, 2010, **12**, 3419-3421.
12. D. Bekermann, A. Gasparotto, D. Barreca, A. Devi, R. A. Fischer, M. Kete, U. Lavrenčič Štangar, O. I. Lebedev, C. Maccato, E. Tondello and G. Van Tendeloo, *ChemPhysChem*, 2010, **11**, 2337-2340.
13. S.-M. Lam, J.-C. Sin, A. Z. Abdullah and A. R. Mohamed, *Sep. Purif. Technol.*, 2014, **132**, 378-387.
14. S.-M. Lam, J.-C. Sin, A. Z. Abdullah and A. R. Mohamed, *J. Colloid Interface Sci.*, 2015, **450**, 34-44.

15. D. Barreca, A. Gasparotto, C. Maccato, E. Tondello, U. L. Štangar and S. R. Patil, *Surf. Coat. Technol.*, 2009, **203**, 2041-2045.

16. N. Todorova, T. Giannakopoulou, K. Pomoni, J. Yu, T. Vaimakis and C. Trapalis, *Catal. Today*, 2015, **252**, 41-46.

17. Y. Huang, C. Guo, L. Huang, Q. Dong, S. Yin and T. Sato, *Int. J. Nanotechnol.*, 2013, **10**, 30-37.

18. A. Di Paola, E. García-López, G. Marcì and L. Palmisano, *J. Hazard. Mater.*, 2012, **211**, 3-29.

19. Y. Wang, Q. Wang, X. Zhan, F. Wang, M. Safdar and J. He, *Nanoscale*, 2013, **5**, 8326-8339.

20. M. Azam Mohd Adnan, N. Muhd Julkapli and S. B. Abd Hamid, *Rev. Inorg. Chem.*, 2016, **36**, 77-104.

21. D. Li, H. Haneda, N. Ohashi, S. Hishita and Y. Yoshikawa, *Catal. Today*, 2004, **93**, 895-901.

22. B. Subash, A. Senthilraja, P. Dhatshanamurthi, M. Swaminathan and M. Shanthi, *Spectrochim. Acta, Part A*, 2013, **115**, 175-182.

23. R. Sugrañez, J. Balbuena, M. Cruz-Yusta, F. Martín, J. Morales and L. Sánchez, *Appl. Catal., B*, 2015, **165**, 529-536.

24. J. Balbuena, G. Carraro, M. Cruz, A. Gasparotto, C. Maccato, A. Pastor, C. Sada, D. Barreca and L. Sanchez, *RSC Adv.*, 2016, **6**, 74878-74885.

25. J. Balbuena, M. Cruz-Yusta and L. Sánchez, *J. Nanosci. Nanotechnol.*, 2015, **15**, 6373-6385.

26. S. Adhikari, D. Sarkar and G. Madras, *RSC Adv.*, 2015, **5**, 11895-11904.

27. J. Xie, Z. Zhou, Y. Lian, Y. Hao, X. Liu, M. Li and Y. Wei, *Ceram. Int.*, 2014, **40**, 12519-12524.

28. S. Adhikari and D. Sarkar, *Mater. Res. Bull.*, 2015, **72**, 220-228.

29. A. J. T. Naik, I. P. Parkin and R. Binions, *IEEE Sens. J.*, 2014, **14**, 3137-3147.

30. Y. Wang, L. Cai, Y. Li, Y. Tang and C. Xie, *Physica E*, 2010, **43**, 503-509.

31. C. V. Ramana, S. Utsunomiya, R. C. Ewing, C. M. Julien and U. Becker, *J. Phys. Chem. B*, 2006, **110**, 10430-10435.

32. M. Saleem, M. F. Al-Kuhaili, S. M. A. Durrani, A. H. Y. Hendi, I. A. Bakhtiari and S. Ali, *Int. J. Hydrogen Energy*, 2015, **40**, 12343-12351.

33. D. Li and H. Haneda, *J. Photochem. Photobiol., A*, 2003, **160**, 203-212.

34. C. Janáky, K. Rajeshwar, N. R. de Tacconi, W. Chanmanee and M. N. Huda, *Catal. Today*, 2013, **199**, 53-64.

35. Y. Liu, H. He, J. Li, W. Li, Y. Yang, Y. Li and Q. Chen, *RSC Adv.*, 2015, **5**, 46928-46934.

36. A. Afzal, N. Cioffi, L. Sabbatini and L. Torsi, *Sens. Actuators, B*, 2012, **171**, 25-42.

37. K. Wetchakun, T. Samerjai, N. Tamaekong, C. Liewhiran, C. Siriwong, V. Kruefu, A. Wisitsoraat, A. Tuantranont and S. Phanichphant, *Sens. Actuators, B*, 2011, **160**, 580-591.

38. Z.-X. Cai, H.-Y. Li, X.-N. Yang and X. Guo, *Sens. Actuators, B*, 2015, **219**, 346-353.

39. C. Zhang, M. Debliquy, A. Boudiba, H. Liao and C. Coddet, *Sens. Actuators, B*, 2010, **144**, 280-288.

40. D. Barreca, G. Carraro, A. Gasparotto, C. Maccato, T. Altantzis, C. Sada, K. Kaunisto, T.-P. Ruoko and S. Bals, *Adv. Mater. Interfaces*, 2017, **4**, 1700161.

41. J. L. Yang, S. J. An, W. I. Park, G. C. Yi and W. Choi, *Adv. Mater.*, 2004, **16**, 1661-1664.

42. A. Gasparotto, G. Carraro, C. Maccato and D. Barreca, *Phys. Status Solidi A*, 2017, **214**, 1600779.

43. D. Barreca, G. Carraro, A. Gasparotto, C. Maccato, C. Sada, E. Bontempi, M. Brisotto, O. Pliekhova and U. L. Štangar, *Environ. Sci. Pollut. Res.*, 2016, **23**, 20350-20359.

44. D. Briggs and M. P. Seah, *Practical surface analysis: Auger and X-ray photoelectron spectroscopy*, John Wiley & Sons: New York, 2nd ed., 1990.

45. M. E. A. Warwick, D. Barreca, E. Bontempi, G. Carraro, A. Gasparotto, C. Maccato, K. Kaunisto, T. P. Ruoko, H. Lemmetyinen, C. Sada, Y. Gonullu and S. Mathur, *Phys. Chem. Chem. Phys.*, 2015, **17**, 12899-12907.

46. U. Černigoj, M. Kete and U. L. Štangar, *Catal. Today*, 2010, **151**, 46-52.

47. N. Vodišek, K. Ramanujachary, V. Brezová and U. Lavrenčič Štangar, *Catal. Today*, 2017, **287**, 142-147.

48. G. Carraro, A. Gasparotto, C. Maccato, E. Bontempi, F. Bilo, D. Peeters, C. Sada and D. Barreca, *CrystEngComm*, 2014, **16**, 8710-8716.

49. Pattern No. 36-1451, JCPDS, 2000.

50. J. F. Moulder, W. F. Stickle, P. E. Sobol and K. D. Bomben, *Handbook of X-ray photoelectron spectroscopy*, Perkin Elmer Corporation, Eden Prairie, MN, USA, 1992.

51. D. Bekermann, A. Ludwig, T. Toader, C. Maccato, D. Barreca, A. Gasparotto, C. Bock, A. D. Wieck, U. Kunze, E. Tondello, R. A. Fischer and A. Devi, *Chem. Vap. Deposition*, 2011, **17**, 155-161.

52. D. Bekermann, A. Gasparotto, D. Barreca, C. Maccato, M. Rossi, R. Matassa, I. Cianchetta, S. Orlanducci, M. Kete and U. L. Štangar, *Cryst. Growth Des.*, 2012, **12**, 5118-5124.

53. R. S. Vemuri, M. H. Engelhard and C. V. Ramana, *ACS Appl. Mater. Interfaces*, 2012, **4**, 1371-1377.

54. H. Ishihara, G. K. Kannarpady, K. R. Khedir, J. Woo, S. Trigwell and A. S. Biris, *Phys. Chem. Chem. Phys.*, 2011, **13**, 19553-19560.

55. G. Hai, J. Huang, L. Cao, Y. Jie, J. Li, X. Wang and G. Zhang, *J. Alloys Compd.*, 2017, **690**, 239-248.

56. A. A. Scalisi, R. G. Toro, G. Malandrino, M. E. Fragalà and G. Pezzotti, *Chem. Vap. Deposition*, 2008, **14**, 115-122.

57. J. Yang, H. Jia, X. Lv and Y. Wang, *Ceram. Int.*, 2016, **42**, 12409-12413.

58. L. I. Ali, S. A. El-Molla, M. M. Ibrahim, H. R. Mahmoud and M. A. Naghmash, *Opt. Mater.*, 2016, **58**, 484-490.

59. S. C. Dhanabalan, J. P. Garcia, D. Calestani, F. Pattini, F. Bissoli, M. Villani, S. Rampino and A. Zappettini, *Cryst. Res. Technol.*, 2014, **49**, 558-563.

60. C. Yu, K. Yang, Q. Shu, J. C. Yu, F. Cao and X. Li, *Chinese J. Catal.*, 2011, **32**, 555-565.

61. A. Yamamoto, Y. Mizuno, K. Teramura, S. Hosokawa and T. Tanaka, *ACS Catal.*, 2015, **5**, 2939-2943.

62. R. Lewis and N. Sax, *Sax's Dangerous Properties of Industrial Materials*, New York, 12th edn., 2012.

63. G. Carraro, R. Sugrañez, C. Maccato, A. Gasparotto, D. Barreca, C. Sada, M. Cruz-Yusta and L. Sánchez, *Thin Solid Films*, 2014, **564**, 121-127.